Exploring the high-temperature frontier in molecular nanomagnets: the case of uranocenium.

Luis Escalera-Moreno,[a] José J. Baldoví,[b]* Alejandro Gaita-Ariño,[a] Eugenio Coronado[a]*

a Instituto de Ciencia Molecular (ICMol), Universidad de Valencia, C/ Catedrático José Beltrán, 2, E-46980 Paterna, Spain.

E-mail: eugenio.coronado@uv.es

b Max Planck Institute for the Structure and Dynamics of Matter, Luruper Chaussee, 149, D-22761 Hamburg, Germany.

E-mail: jose.baldovi@mpsd.mpg.de

KEYWORDS single-ion magnets, magnetic relaxation, spin-phonon coupling, uranocenium

Supporting Information Placeholder

ABSTRACT: Molecular nanomagnets based on mononuclear metal complexes, also known as single-ion magnets (SIMs), are crossing challenging boundaries in Molecular Magnetism. From a experimental point of view, this class of magnetic molecules has expanded from lanthanoid complexes to transition metal complexes and, more recently, to actinoid complexes. From a theoretical point of view, more and more improved models have been developed and we are now able not only to calculate the electronic structure of these systems on the basis of their molecular structure, but even to unveil the role of vibrations in the magnetic relaxation processes, at least for lanthanoid and transition metal SIMs. This knowledge has allowed to optimize the behavior of dysprosocenium based SIMs until obtaining magnetic hysteresis above liquid-nitrogen temperature. In this contribution we cross a new boundary by extending the theoretical modelling of the vibrationally-induced spin relaxation to actinoid SIM complexes and, in particular, to uranocenium.

Introduction

The possibility of storing binary information into a single magnetic molecule is a dream that has revolutionized the field of molecular magnetism since the early 1990s. The pursuit of minimalistic magnets exhibiting magnetic hysteresis from purely molecular origin started with the discovery of slow relaxation of the magnetization and macroscopic quantum tunneling of the magnetization in $[Mn_{12}O_{12}(O_2CMe)_{16}(H_2O)_4]\cdot 2MeCO_2H\cdot 4H_2O$ ($Mn_{12}ac$),[1,2] popularly known as the *drosophila* of the single-molecule magnets (SMMs).[3] This class of magnetic entities exhibit magnetic bistability generated by an energy barrier to the magnetization reversal. Because of their extraordinarily rich physical behavior, SMMs have been considered as ideal laboratories to study new quantum phenomena,[4] such as quantum tunneling of the magnetization, while they are also potential candidates for a set of stimulating applications.[5,6,7,8] The main figure of merit that evaluates the performance of an SMM is the blocking temperature (T_b), which can be described as the highest temperature at which these nanomagnets can retain its magnetization for a given time interval. The enhancement of T_b has then been the main target for researchers aiming at obtaining SMMs exhibiting magnetic hysteresis at high temperature. The first generation of SMMs was based on magnetic transition metal clusters, in which an anisotropic high-spin ground state can be stabilized by superexchange interactions between a number of anisotropic magnetic centers. Despite the great attention that this kind of nano-objects attracted, the progress with regard to their energy barrier (U_{eff}) and T_b was pretty modest because

of the intrinsic limitations to increase the height of the anisotropy barrier.[9] Among this wide variety of transition metal clusters, the two record-bearing families are the $\{Mn^{III}_8Mn^{IV}_4\}$ SMMs, derived from the original Mn_{12}ac, which present U_{eff} values as large as 74 K,[10,11] and the $\{Mn^{III}_6\}$-oximato clusters that possess practically the same record energy barrier with $[Co_4(\mu\text{-}NPtBu_3)_4][B(C_6F_5)_4]$ (where ^tBu = tert-butyl), being 86 K for $\{Mn_6\}$[12] and 87 K for $\{Co_4\}$[13]. In 2003, a novel framework to design SMMs was introduced by Ishikawa and co-workers.[14] This resulted in the development of even smaller nanomagnets based on coordination compounds with a single lanthanoid ion as the source of magnetic anisotropy, which arise from the combination of unquenched spin-orbit and ligand field.[15] The first example of this second generation of SMMs relies on a terbium cation sandwiched by two phthalocyaninato anions. This system represented an important increase of the energy barrier (U_{eff} = 330 K), but its blocking temperature was merely 1.7 K. Since then, a vast number of mononuclear SMMs, also known as single-ion magnets (SIMs), have been reported.[16] The discovery of single-ion magnetism based on lanthanides stimulated the quest for this behavior in other types of magnetic ions in the periodic table. Still, less effort has been put so far into this direction compared with the impressive expansion of the lanthanoid-based family, and thus a considerable smaller number of examples exist. As far as the transition metal based SIMs are concerned, dozens of examples have been reported,[17] and while cobalt and iron are the most common magnetic ions, examples also include chromium, manganese, nickel, copper and rhenium.[18] Despite this synthetic effort, the hysteresis record in standard conditions for transition metal mononuclear SMMs is still the one of the first reported example, namely 6.5 K for [K(crypt-222)][$Fe(C(SiMe_3)_3)_2$], which displays an energy barrier of 226 cm^{-1}.[19] Also, note that magnetic hysteresis with coercivity was measured for [(SIPr)Co=NAr] (SIPr = 1,3-bis(2,6-diisopropylphenyl)imidazolin-2-ylidene, and Ar = 2,6-dimesitylphenyl) up to 9.5 K using a fast field sweep rate of 700 $Oe{\cdot}s^{-1}$.[20] In actinides, both the number and the variety of examples are remarkable smaller compared to the case of transition metals. Practically all of the studied systems are based on uranium,[21,22,23] with only a couple of examples based on neptunium[24] and plutonium. The best reported case is the uranium complex [$U(TpMe_2)_2$]I with hysteresis below 5 K.[25]Owing to [26]the broader number of available SIMs based on the lanthanoid-based family and to the accumulation of knowledge derived from the theoretical studies, improved design strategies have been developed to improve their properties. A key example that illustrates this point is provided by the cyclooctatetraenyl metallocene complexes in linear coordination. Thus, a wise choice of the lanthanoid has allowed to maximize the anisotropy achieving blocking temperatures as high as 14 K in the Er^{3+} derivatives.[27] This strategy has subsequently been improved using more compact π-clouds and thus a stronger axial magnetic field, which has resulted in a dramatic ramp-up of T_b since 2017, with the chemical design of SIMs reaching magnetic hysteresis above liquid-nitrogen temperatures (see Fig. 1). Up to now, the most promising systems have been double-decker systems based on rigid aromatic rings. This kind of coordination environment, which depend on the selected rings, favors an axially-elongated ligand field that encapsulates a lanthanide ion with an oblate *f*-shell cloud, e.g. Dy^{3+}, which minimizes electrostatic repulsion. By a careful tailoring of the substituents in this type of aromatic ligands, one can envision further improvements beyond the current performances of these magnetic entities that are nowadays the high-temperature frontier of SIMs.

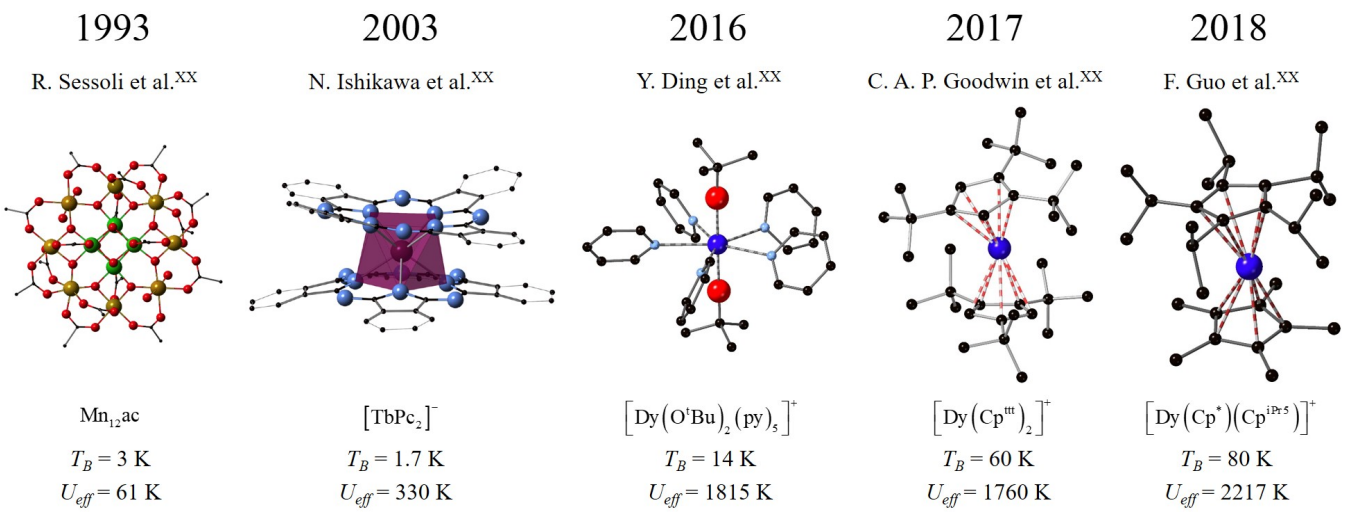

Fig 1. Milestones in single-ion magnets of rising values of effective barriers U_{eff} and blocking temperatures T_b.

Modeling the electronic structure in f-block single-ion magnets

Despite this encouraging progress, modeling the properties of *f*-block molecular nanomagnets from accurate magneto-structural correlations is considered a great challenge that awakes a remarkable interest in the field. Nowadays, there are several complementary methodologies that have been progressing in parallel with respect to the experimental discoveries. There is an upward trend in molecular magnetism to standardize on methods based on the chemical structure, either electrostatic or, more commonly, *ab initio*. In contrast, spectroscopists studying the optical transitions of the rare earths tend to rely on phenomenological crystal field methods, fitting a large range of experimental energy levels.

The current theoretical and computational tools to estimate the energy barrier have been mainly focused on lanthanoid SIMs. These approaches are based on previous theoretical results developed for lanthanide ions embedded in solid-state matrices or in highly symmetric inorganic crystal field environments. At the same time, the computational tools to calculate the joint effect of spin-orbit coupling and the ligand field -such as methods based on the Complete Active Space but including spin-orbit coupling as a perturbation- had been used in molecular magnetism for the study of spin states in magnetic molecules exhibiting anisotropy. Because of the historical importance of transition metals in molecular magnetism, this originally often meant calculating the effective Landé *g* parameter.[28] However, as soon as transition metal SIMs were a reality, CASSCF-based methods were applied to them.[29,30] In contrast, DFT methods, which had been used with some success to rationalize the effective barrier in (Mn_{12}ac), have not been commonly employed in the case of SIMs,[31] so we will not focus on them here and instead review the difference between electrostatic crystal-field models, which have been applied frequently in this field, and post Hartree-Fock multi-configurational *ab initio* methodologies, which have been used even more extensively.

Electrostatic crystal-field models aim to describe the perturbation of the 4*f*-shell

electron cloud of the central ion produced by a surrounding charge distribution that breaks the degeneracy within the ground *J* multiplet. The simplest model of this type is the Point Charge Electrostatic Model (PCEM), in which the electrostatic field is parameterized as a sum of Coulomb fields created by point charges (i.e. the formal charges) placed at the crystallographic positions, completely disregarding covalency.[32] In molecular magnetism, this basic but intuitive idea permitted a preliminary attempt to rationalize the most likely conditions that lanthanoid-based complexes need to meet to behave as SIMs, both qualitatively[33] and quantitatively.[34,35] Based on the PCEM, the MAGELLAN code was developed as an inexpensive tool for the easy axis direction of low-symmetry dysprosium SIMs in 2013.[36] Since the middle of last century, a plethora of modifications of this early model have been suggested in the literature.[37,38,39,40,41] The idea has been to keep the simplicity of PCEM to some extent, but providing a more realistic set of CFPs as the spectroscopic techniques allowed a better estimation of them. Among those improvements, the Radial Effective Charge (REC) proposed by our group has often been used for the inexpensive modeling of molecular nanomagnets[42] and spin qubits,[43] The essential change of the REC model is the substitution of the formal charges of the atoms in the first coordination sphere by effective charges that are smaller than the real charges and are placed at smaller distances from the metal to account for covalency. For that, two parameters per type of donor atom are defined, namely the effective charge (Z_{eff}) and the radial displacement (D_r). In a fitting procedure, both REC parameters are varied to achieve the minimum deviation between calculated and experimental data. The displacement of the point charge along the chemical bond direction has remarkable consequences in the values of the second-, fourth- and sixth-rank CFPs, correcting the deviations that had historically been encountered when comparing the PCEM-derived CFPs with phenomenological ones.[44]

On the other hand, recent advances in post Hartree-Fock multi-configurational *ab initio* methodologies have permitted to develop a computational framework that has widely been used in the theoretical characterization of these magnetic entities. The main difference with regard to *semi-empirical* or phenomenological methods is that *ab initio* approaches do not rely on experimental data to be fitted. This means that their results are derived from the fundamental constants introduced by the applied quantum physical laws. Thus, it provides a perfect scenario to correlate the chemical structure with the magnetic and spectroscopic properties limited instead by computational time consumption. The most broadly employed *ab initio* multi-configurational approach is the CASSCF/PT2 method (Complete Active Space Self-Consistent Field and Perturbation Theory up to Second Order), subsequently complemented with spin-orbit interaction effects (e.g. RASSI-SO, Restricted Active Space State Interaction with Spin-Orbit coupling).[45,46,47] This method has been implemented in a plethora of computational packages such as MOLCAS –the most historically used in molecular magnetism–,[48,49] Gaussian,[50] Orca[51] and MOLPRO[52]. It allows the calculation of the full set of CFPs, energy levels, wave functions, as well as the orientation of the main magnetic axes and the static magnetic properties. The basics of this approach has deeply been described in the literature. Very recently, simplifications to CASSCF via the configuration-averaged Hartree-Fock (CAHF) algorithm with the objective of achieving similar results that those of CASSCF while reducing the time-scale of the calculations have been proposed.[53,54] The CASSCF/RASSI-SO method has played a determinant role in the understanding of the static magnetic properties of molecular nanomagnets and spin qubits. Through the SINGLE_ANISO program, it has been possible to compute magnetic anisotropy,[55] magnetic susceptibility, magnetization, energy levels, magnetic relaxation pathways[56] and magnetic couplings,[57] as well as the full set of 27 CFPs.[58] In this approach, CFPs are deduced by a decomposition of the CF matrix in irreducible tensor operators (ITOs) and in extended Stevens operators working in the ground $^{2S+1}L_J$ multiplet. Simultaneously, the projections of the total angular momentum with respect to the reference coordinate frame are also estimated. The first remark-

able application of *ab initio* methods to a mononuclear SMM dates back to 2012, when CASPT2 calculations were able to simulate the magnetic anisotropy changes of $[Na\{Dy(DOTA)(H_2O)\}]\cdot 4H_2O$, derived by the rotation of the apical water molecule of the complex.[59,60] Soon, this approach became very popular –one can find near a hundred of relevant results from Web of Science concerning mainly the application of CASSCF in *f*-element molecular magnetism–, and its success in the prediction of magnetic anisotropy, especially in Dy complexes, has been demonstrated again and again.

The next frontier in the rationalization and modeling of *f*-block molecular nanomagnets is the application of the above-mentioned theoretical frameworks to the study of actinoid-based SIMs. This kind of systems have been considered as very promising in molecular magnetism because actinides can, in principle, combine the best features of 3d and 4f nanomagnets, since 5f electrons can lead to the simultaneous presence of strong magnetic anisotropy and magnetic superexchange coupling with other magnetic centers. Unfortunately, this promise is largely hindered by the complexity that they present for their modeling, thus difficulting a rational design of actinoid-based SIMs exhibiting improved properties. Due to the larger crystal field splitting that this type of complexes do possess, one needs to define a "full model" Hamiltonian taking into account inter-electronic repulsion, spin-orbit coupling and the ligand field potential.[61] In this context, the CONDON package appears as the leading software code for this modeling. The best strategy is to provide an initial guess of the CFPs using either electrostatic or *ab initio* methods and then diagonalize the full Hamiltonian or fit a series of experimental energy levels by varying the calculated CFPs In any case, one should note that in uranium, perhaps even more than with lanthanides, there is a large mismatch between U_{eff} and energy gaps, of one to two orders of magnitude.[62] This means that a simple Orbach process cannot describe the behavior properly and has stimulated some authors to assume a Raman process. Meihaus *et al.* showed that the temperature-dependent data of many U^{3+}-SIMs might be fit well to a power dependence of temperature.[63] This serves as a powerful stimulus for a more detailed modelling of the vibrationally-induced relaxation in actinides.

Modeling the effect of vibrations on single-ion magnets

One of the most recent crucial advances in this context, from the theoretical point of view, has been the incorporation of the effect of both molecular and lattice vibrations that couple to the spin states into the computational methodologies (see Fig. 2). Indeed, the quantitative improvement between the complex known as $[Dy(Cp^{ttt})_2]^+$ (T_b = 60 K)[64] and Dy-5* (T_b = 80 K) was justified as a rational optimization of the molecular structure in terms of vibrations.[cita Layfield **] Since the hydrogen atoms in the Cp rings were involved in the vibrations that contributed most to the Orbach relaxation, these were substituted by aliphatic groups. This, of course, required a judicious design to find the exact steric impediment that allows coordination to the Dy of two substituted Cp rings while impeding a third ligand to join the coordination sphere. In this case, achieving this compromise while eliminating any hydrogen atom directly connected to the Cp rings meant overcoming the synthetic complication of combining two different rings, one with bulky isopropyl groups and another with the smaller methyl groups. Moreover, the theoretical analysis of Layfield and coworkers indicates that two out-of-plane vibrations of the Cp* ligand with frequencies in the range of the calculated gap to the first excited state (about 650 cm^{-1}) might be responsible for relaxation in Dy-5*, thereby indicating the direction for further improvements: choosing substituents to bring these modes out of resonance with the excitation gap.

As in the case of the modeling of the ligand field, the modeling of the coupling between vibrations and spin energy levels also started with transition metals.[65] A contribution by some of us introduced one of the germinal ideas on which current models rely on,[66] already in 2015: Based on the case study of the square planar complex $[Cu(mnt)_2]^{2-}$ (mnt^{2-} = 1,2-dicyanoethylene-1,2-dithiolate), this was a systematic procedure to estimate the coupling between the electron spin energy levels and each individual molecular vibrational mode. This model relies on the ability to calculate, for any given geometry, the parameter *B* in the Hamiltonian that governs spin energy levels, such as the effective Landé *g* factor, the Zero Field Splitting *E* or the set of CFPs $\left\{B_2^0 \ldots B_6^6\right\}$. By preparing molecular geometries along the distortion coordinate Q_k of each vibrational mode k, by re-calculating this parameter *B* for each of these coordinate sets, and by assuming a vibrational harmonic model, a Taylor expansion up to second order in mode coordinates leads to a simple expression for the coupling of *B* with each mode *k* as a function of the vibrational frequency of the mode, its reduced mass, and the second derivative of *B* with respect to Q_k evaluated at the relaxed geometry. It is important to note that this early model did not yet calculate relaxation times but merely matrix elements for the future master equations.

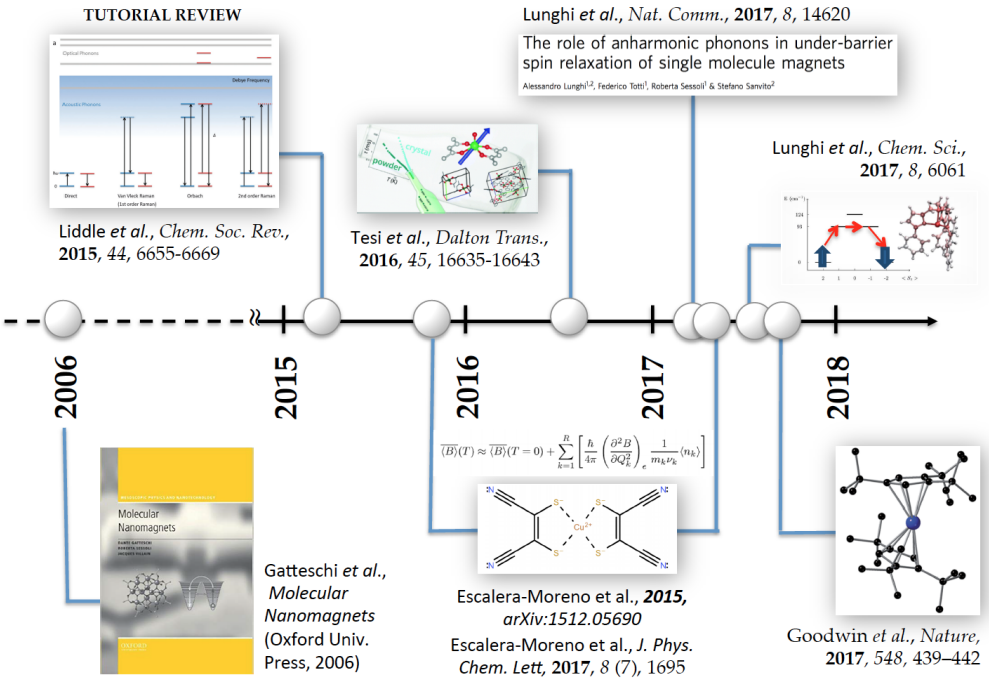

Fig 2. Milestones in the theoretical modeling of vibration-mediated spin relaxation in molecular nanomagnets.

In 2017, a more sophisticated work was developed by Lunghi and co-workers, based on the trigonal complex $[(tpaPh)Fe]^{-}$ (tpa=tris(pyrrolyl-R-methyl)amine).[67] This contribution introduced a series of new key concepts into this research line, allowing to apply a correction to the Arrhenius plots and to explain why for high barrier cases the effective barrier can be much lower. Working under the Born–Markov approximation, the authors integrate out the phonons' component of the density matrix and reduce the problem to a purely electronic one in the presence of a phonon bath. The spin dynamics are then studied through the first-order-reduced spin density operator as described by the diagonal elements of the Redfield master equation, where phonon dissipation is explicitly introduced by modeling their spectral shape. Indeed, this model considers the phonon linewidth Δ that, after a threshold temperature, scales linearly with temperature. Importantly, this linewidth serves to explain the role of anharmonic phonons to achieve the resonance condition and ultimately the transfer of energy from an excited spin state towards the phonon thermal bath. Since the authors in this contribution solve the master equation, an estimate of the full relaxation time is calculated as a function of temperature. This work was accompanied by related advances by the same authors, which demonstrate the importance of local vibrational modes in magnetic relaxation,[68] and correlate their harmonic frequencies with experiments from THz spectroscopy.[69] Late progress on this line includes further first-principle spin dynamics by analyzing the role of coordination geometry and ligand field strength.[70] In the case of vanadyl complexes, the relaxation mechanism is dominated, depending on whether the magnetic field is low or high, by the modulation of hyperfine coupling or of the Zeeman effect by the intra-molecular components of the acoustic phonons.[71]

After the ground was set by studies in transition metal complexes, the modeling of the coupling between vibrations and spin energy levels in lanthanide ions was finally kick-started by the two recent records in high-temperature magnetic hysteresis, both based on the chemical family of the dysprosocenium sandwich.[Goodwin-Nature-2017],[F.-S. Guo, B. M. Day, Y. C. Chen, M.-L. Tong, A. Mansikkamäki, R. A. Layfield, *Science*, 2018, 362, 1400-1403] In both cases, the spin–phonon coupling was determined

by performing an extensive series of CASSCF-SO calculations for molecular geometries distorted along each vibrational mode. The variation of the CFPs was subsequently estimated from crystal field decomposition of the electronic structure for each of the distorted structures. One major approximation common to both works, namely to ignore long-wavelength phonons and to focus only on gas-phase local vibrations, may suppose an important limitation. A recent theoretical work provided preliminary insight into this open problem by finding –for a different lanthanide complex- that long-wavelength phonons and low-frequency vibrations (below 10 cm^{-1}) do not modulate significantly the spin energy levels in the solid state.

Crucially, Goodwin and co-workers (**ref**) went a step further and re-defined vibrationally-induced Orbach and second-order Raman transition rates between two given electronic states. By assuming the Born-Oppenheimer approximation and a harmonic vibrational perturbation to the equilibrium electronic structure, the new expressions depend on a finite set of non-interacting harmonic vibrations as provided by first-principles geometry relaxations, instead of the common vibrational energy continuum derived from the use of the Debye model. These expressions allow building the so-called master matrix, whose diagonalization results in a series of characteristic relaxation rates that describe the several relaxation channels of the system. In particular, when the Orbach transition rates are employed, all but one are fast relaxation rates corresponding to processes at either side of the barrier, and the remaining slow relaxation rate corresponds to the Orbach relaxation over the barrier.

The uranocenium family is the latest unexplored frontier in this challenging effort, since it combines the difficulties for the modeling of the electronic structure in actinide coordination compounds, as detailed in the previous section, with a scarcity in experimental results. However, at the same time, this family may could extend the promise of the hysteresis records experimentally found for dysprosocenium complexes under a rational design.

The uranocenium case: Spin-vibrational coupling and calculated magnetic relaxation dynamics

In order to explore the spin-vibrational coupling in a foreseeable actinoid-based SIM with a large energy barrier we are going to focus on the uranocenium complex. Since metallocenium-based complexes hold the latest records in blocking temperature T_b, [ref **] we probed the (hypothetical) uranium analogue of $[Dy(Cp^{ttt})_2]^+$ (T_b = 60 K), [ref**] namely, $[U(Cp^{ttt})_2]^+$, see Fig. 3. Hereafter, we must again bear in mind both the main current motivation and the ultimate goal of the corresponding first-principles calculations. First, the low operating temperatures of molecular nanomagnets still hamper their implementation in devices working at more practical temperatures. Second, the pursuit of high-temperature molecular magnets involves taking care about new relaxation mechanisms that start to dominate demagnetization at high enough temperatures. Indeed, as temperature is raised, the increasing energy stored in the phonon bath can now promote the nanomagnet relaxation, by which the spin makes use of this thermal energy and crosses a potential barrier to be finally reversed. This particular process is possible because of the so-called spin-vibration coupling. Thus, any attempt to rationalize and predict new molecular magnets operating at high temperatures needs to necessarily understand the interaction between spins and vibrations. In particular, the current theoretical efforts are essentially aimed at identifying those molecular vibrations responsible for the nanomagnet demagnetization. Subsequently, the molecular ligands can be re-designed in order to suppress the relevant atomic movements that significantly couple to the spin and promote its relaxation. As explained above, this is the strategy that was succesfully applied in $[Dy(Cp^{ttt})_2]^+$ to increase its blocking temperature from 60 K to 80 K in the latest reported dysprosocenium complex.[ref**]

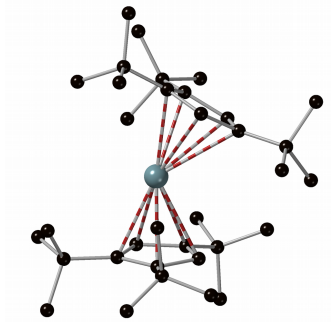

Fig. 3. Relaxed geometry of $[U(Cp^{ttt})_2]^+$, where hydrogen atoms have been omitted for clarity.

When studying vibration-mediated relaxation in nanomagnets, the general scheme currently employed from the theoretical side consists in the following simple picture: an equilibrium electronic structure, in the form of a potential barrier where the spin is initially located at one side, perturbed by a set of harmonic molecular vibrations whose coupling reverse the spin after crossing the barrier. To determine the equilibrium electronic structure, one first has to relax the molecular geometry. This means to reach a minimum in the potential energy surface as a function of the atom coordinates. At this relaxed geometry, the CFPs are estimated and their implementation in the crystal field Hamiltonian determines the equilibrium electronic structure. The estimation of the equilibrium CFPs can be accomplished by means of a standard CASSCF calculation. [ref] Since this is not possible in our case as we lack an experimental geometry of $[U(Cp^{ttt})_2]^+$, we use the equilibrium electronic structure of $[Dy(Cp^{ttt})_2]^+$ as a starting point and project it onto $[U(Cp^{ttt})_2]^+$.[arxiv**] This projection leads to equilibrium electronic structure as shown in Fig. 4.

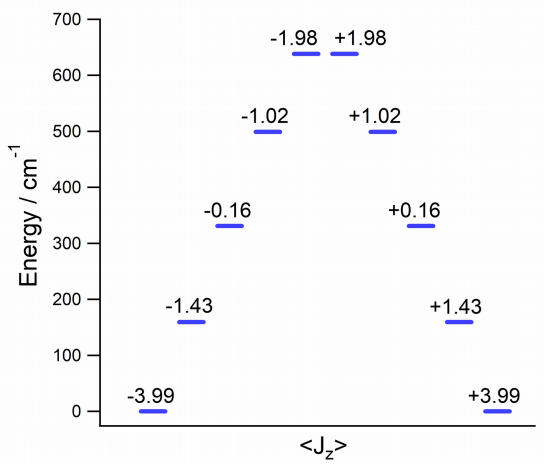

Fig. 4. Lowest $2J+1$ electron spin states of the ground $J = 9/2$ multiplet of U^{3+} evaluated at the relaxed geometry of $[U(Cp^{ttt})_2]^+$, along with the J_z expectation values.

Once the molecular geometry has been fully relaxed, the next step is the calculation of its vibrational spectrum. This step provides the set of molecular vibrations in the form of the following information: harmonic frequencies ν_j, reduced masses m_j and displacement vectors. For each vibrational mode, these vectors determine the direction along which each atom vibrates around its relaxed position. The vibrational perturbation on the equilibrium electronic structure is introduced by calculating the change in each equilibrium crystal field parameter produced by the action of each vibrational mode. In a previous work we calculated this change up to second order in mode coordinate Q_j and as a function of temperature T.[jpcl**] This change $\Delta\left(A_k^q\langle r^k\rangle\right)_j(T)$, in terms of Stevens notation, depends on the j vibrational mode and on the crystal field parameter k,q as displayed in Eq. (1):

$$\Delta\left(A_k^q\langle r^k\rangle\right)_j(T)=\frac{\hbar}{4\pi}\left(\frac{\partial^2 A_k^q\langle r^k\rangle}{\partial Q_j^2}\right)_{eq}\frac{1}{m_j\nu_j}\left(\langle n_j\rangle+\frac{1}{2}\right)$$

(1)

The variable $\langle n_j\rangle=1/\left(\exp\left(h\frac{\nu_j}{K_BT}\right)-1\right)$ is the so-called boson number. It accounts for the thermal dependence of $\Delta\left(A_k^q\langle r^k\rangle\right)_j(T)$ and describes the average number of available vibration quanta at a given tempera-

ture in the mode *j*. Another important variable in Eq. (1) is the second derivative of $A_k^q\langle r^k\rangle$ respect to Q_j evaluated at the relaxed geometry. Its determination is straightforward and can be found elsewhere.[jpcl**] Crucially for our interest, the spin-vibration coupling matrix elements $\langle i|\widehat{H}|f\rangle$, which compose the transition rates γ and connect two given states $\text{¿}i\rangle$ and $\text{¿}f\rangle$ in Fig. 4, depend proportionally on Eq. (1) through the perturbing Hamiltonians $\widehat{H}_j$ in Eq. (2):

$$\widehat{H}_j = \sum_{k=2,4,6} \sum_{q=-k}^{k} \Delta\left(A_k^q\langle r^k\rangle\right)_j(T)\eta_k\widehat{O}_k^q \qquad (2)$$

This perturbing Hamiltonian, which is different for each mode *j*, is written in terms of the extended Stevens operators $\widehat{O}_k^q$ and the Stevens coefficients. Since our selected *f*-block metal is U^{3+}, we employ the coefficients corresponding to the isoelectronic f^3 metal ion Nd^{III}.

At this point, we can already state the key role of Eq. (1) in relation to magnetic relaxation. Indeed, the evaluation of this relaxation depends on solving a master equation, which determines the time evolution of the spin population through the several states in Fig. 4. A commonly employed equation is the so-called Pauli master equation, which is the one we can use to model the vibration-induced relaxation in $[U(Cp^{ttt})_2]^+$.[72] This equation depends on the abovementioned transition rates, which consist in a summation of independent contributions each one accounting for a different vibrational mode. The key point is that each one of these contributions is proportional to the corresponding matrix element $\langle i|\widehat{H}|f\rangle$. Thus, since $\widehat{H}_j$ is also proportional to Eq. (2), in order to suppress the transition rates and, consequently, the magnetic relaxation we need to unavoidably look for strategies aimed to cancel each $\Delta\left(A_k^q\langle r^k\rangle\right)_j(T)$. From Eq. (2), one can already realize that a proper increase both in the harmonic frequency ν_j and in the reduced mass m_j will lead to a reduction in $\Delta\left(A_k^q\langle r^k\rangle\right)_j(T)$. In addition, a complementary and beneficial effect is that of those modes that give a quasi-linear evolution in $A_k^q\langle r^k\rangle$ with Q_j around the relaxed geometry, since these modes will produce a rather negligible second derivative in Eq. (2). [jpcl**]

The Pauli master equation is a linear differential equation. Thus, to solve it one only needs to diagonalize its coefficient matrix known as master matrix. These coefficients are nothing but the several transition rates that connect each pair of spin states in Fig. 4. The diagonalization of this matrix provides the different relaxation rates corresponding to the different spin relaxation channels as mentioned above. One of these rates is in fact strictly zero, and represents the situation of thermal equilibrium. This situation is attained at infinite time, and the spin population of each state is distributed according to the Boltzmann law. All but one of the other channels corresponds to spin motions on either side of the potential barrier, and are characterized by fast relaxation rates. The remaining channel corresponds to the process by which the spin crosses the barrier until its reversal. Like the picture of a chemical reaction, this process is characterized by a slow relaxation rate and represents the rate-determining step in the nanomagnet relaxation. Thus, this slow rate τ^{-1} determines the timescale of the nanomagnet demagnetization at the working temperature *T*. In Fig. 5 we show our calculated thermal evolution of the relaxation time τ for $[U(Cp^{ttt})_2]^+$ by employing the Orbach transition rates in the master equation. Here we focus on the Orbach process as it commonly dominates magnetic relaxation in the temperature range where the molecular magnetism community is now turning its attention. In fact, we repeated this calculation but by employing the second-order Raman transitions rates and found that this mechanism is far from dominating relaxation in the explored temperature range such as in $[Dy(Cp^{ttt})_2]^+$.

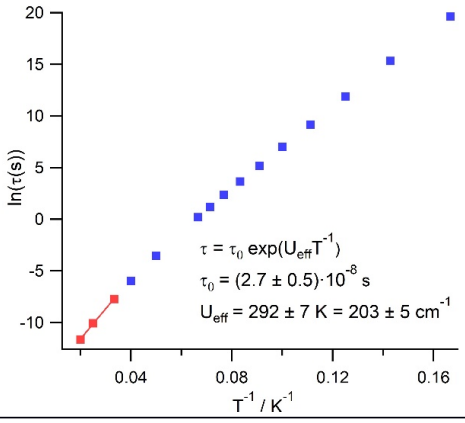

Fig. 5. Temperature dependence of relaxation time τ. The fitting in the range 30-50 K where the Orbach process dominates relaxation corresponds to an Arrhenius-like law.

The relaxation time in the temperature range where the Orbach process dominates (above some few tens of Kelvin) is experimentally modeled by an Arrhenius-like law $\tau = \tau_0 \exp\left(U_{eff}\, T^{-1}\right)$. Thus, the thermal evolution of τ follows a linear trend when plotting ln(τ) vs T^{-1}. In this process, the spin does not necessarily reach the top of the barrier before crossing. Instead, it tunnels the barrier at an effective height given by U_{eff}. The Orbach prefactor τ_0^{-1} represents the number of attempts per unit time to tunnel the barrier. From Fig. 5, the fitting produces the following estimations: U_{eff} = 203 cm^{-1} and τ_0 = 2.7·10^{-8} s. As one can observe in Fig. 4, the effective barrier U_{eff} would be located around 40 cm^{-1} above the first excited doublet in [U(Cp^{ttt})$_2$]$^+$, and lies among the standard values found for a large set of recent molecular magnets.[ref**] The estimated Orbach prefactor is also found inside the experimentally-observed common range 10^{-5}-10^{-10} s.[73]

A complementary information that can also be extracted from the master matrix when using the Orbach transition rates is the relaxation pathway followed by the spin, see Fig. 6. Of course, this should be applied only at those temperatures where the Orbach process is the dominating relaxation mechanism. First, one needs to place all the spin population at a given state in Fig. 4 as an initial condition to solve the master equation. Since our current interest is the use of a molecular magnet as a classical memory storage device, the initial spin population is all placed at one component of the ground doublet, which acts as the memory bit. In an experiment, this corresponds to magnetize the sample in the magnetic anisotropy direction and then to turn the magnetic field off. Below 25 K, we found that only the ground and first excited doublets are populated and the spin tunnels the barrier through their components. Nevertheless, here we must recall again that we are only considering Orbach-driven magnetic relaxation. At low temperatures, alternative relaxation mechanisms can be at play and dominate, such as the case of the direct process where the spin tunnels the barrier through the ground doublet components without populating any excited doublet. Above 25 K, the Orbach process starts to dominate. This is the so-called thermally-activated regime where the number of available phonons is high enough to promote the spin to excited states. As temperature is raised, both the first and second excited doublets become populated, and an increasing spin population tunnels the barrier through their components.

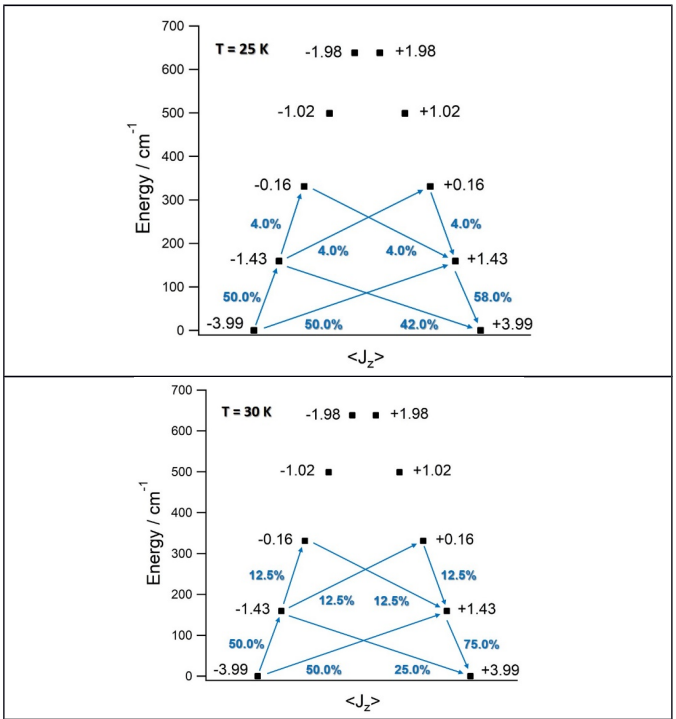

Fig. 6. Orbach-mediated relaxation pathways at different temperatures. All spin population is initially located at the <J_z> = -3.99. The percentages, which represent the fraction of the departing spin populations, are normalized to the incoming spin population of each state.

Final discussion and conclusions

In the above we have calculated the electronic structure and the spin-vibrational coupling in an uranocenium complex namely $[U(Cp^{ttt})_2]^+$. Here these results will be compared with those observed in the lanthanoid analogues as well as in the uranium-based SIMs.

As far as the electronic structure is concerned, an important feature of the equilibrium electronic structure is the composition of the spin states in terms of the $|M_J>$ labels corresponding to the ground J multiplet. In $[U(Cp^{ttt})_2]^+$, the ground doublet is composed in a 82% of $|\pm 9/2>$, being the $|M_J>$ mixing even more noticeable in the excited doublets, see SI. This extensive mixing has also been calculated in the previously reported uranium-based nanomagnets,[74,75] and facilitates magnetic relaxation. Furthermore, as pointed out above (see Figure 6), in $[U(Cp^{ttt})_2]^+$ the spin tunnels the barrier just a bit above the first excited doublet. These features are in sharp contrast with those exhibited by the dysprosocenium magnets $[Dy(Cp^{ttt})_2]^+$ and Dy-5*, where (i) the low-lying spin states are much purer although the ligand coordination is not strictly axial, and (ii) the barrier tunneling is produced close to the most excited doublets. Thus, according with this electronic structure, the SMM performance in $[U(Cp^{ttt})_2]^+$ is expected to be worse than for the dysprosocenium magnets. Still, to confirm this conclusion we must also check the timescale of the relaxation pathway. Indeed, a large enough relaxation time would at least make barrier tunneling through the lowest doublets take longer. We note that the estimated relaxation times in $[U(Cp^{ttt})_2]^+$ are clearly much shorter than those reported for $[Dy(Cp^{ttt})_2]^+$ and Dy-5*. These estimations allow us to predict that the experimental detection limit (: 10^{-6} s) in $[U(Cp^{ttt})_2]^+$ would be reached at 50 K. Compared with the previously reported uranium-based nanomagnets, this upper bound is around one order of magnitude larger.

Inside the thermally-activated regime, where the Orbach process dominates relaxation, an effective barrier of U_{eff} = 292 K is estimated for $[U(Cp^{ttt})_2]^+$, which is clearly below those determined for $[Dy(Cp^{ttt})_2]^+$ (U_{eff} = 1760 K) and Dy-5* (U_{eff} = 2217 K). On the contrary, the calculated Orbach prefactor $\tau_0 = 2.7 \cdot 10^{-8}$ s in $[U(Cp^{ttt})_2]^+$ is at least three orders of magnitude larger than those experimentally found for $[Dy(Cp^{ttt})_2]^+$ ($\tau_0 = 2.0 \cdot 10^{-11}$ s) and Dy-5* ($\tau_0 = 4.2 \cdot 10^{-12}$ s). Thus, the attempt rate to cross the barrier would be much slower in $[U(Cp^{ttt})_2]^+$. The comparison of $[U(Cp^{ttt})_2]^+$ with the previously reported uranium molecular magnets reveals two important points: On one hand, our calculated Orbach prefactor is found among the smallest ones. On the other hand, U_{eff} in $[U(Cp^{ttt})_2]^+$ is estimated in the several hundreds of Kelvin, while this figure of merit has been commonly found in the range of dozens of Kelvin for uranium-based SIMs. (**Ref U16, U17) In conclusion, while it is clear that $[U(Cp^{ttt})_2]^+$ is far from outperforming the lanthanoid analogues $[Dy(Cp^{ttt})_2]^+$ and Dy-5* in terms of magnetic bistabilty, this nanomagnet may represent a significant advance with respect to the uranium-based nanomagnets.

Finally, inspection of the Orbach-based master matrix provides a last and useful information for the molecular design of novel uranium-based nanomagnets. Indeed, once the most-likely relaxation pathway has been identified, the Orbach transition rates that connect the states present in this pathway can be checked. As explained above, these rates depend on the contributions from the different vibrational modes whose energy drives the spin across these states. In these rates, we will focus on those modes with the highest relative weight. Thus, after a visual inspection of them, it will be possible to propose structural modifications in the ligands aimed to suppress the action of these particular vibrations, with the hope of increasing the magnet performance. Among our calculated vibrational modes in $[U(Cp^{ttt})_2]^+$, there exist six of them which have the highest relative weight in the relevant transition rates, see SI. One of these vibrations (16^{th}) was also identified in $[Dy(Cp^{ttt})_2]^+$ (64^{th} and 67^{th}). This is a rocking-like deformation where the hydrogen atoms bounded to the coordinating rings moves towards and away from the metal ion (see **figura animada en SI**). The movement of these hydrogen atoms was eliminated once they were replaced by bulkier substituents in Dy-5*. Intriguingly, this modification succeeded as both the blocking temperature and the effective barrier were increased by 20 K and around 300 cm^{-1}, respectively. There exist two more vibrational modes (18^{th} and 21^{th}) with clearly characteristic movements among those that dominate the relaxation pathway in $[U(Cp^{ttt})_2]^+$. These are breathing-like vibrations where the rigid Cp^{ttt} rings approach and move away from each other (see **figura animada

en SI**). Importantly, they are also present in Dy-5* (66^{th}, 67^{th}, 68^{th}) and could be hindered by stapling the two coordinating rings such as in some bis-phthalocyanines. Other noticeable movements among the remaining important vibrational modes of $[U(Cp^{ttt})_2]^+$ involve methyl rotations in the terc-butyl substituents. Initially, one could partially block these rotations by employing the heavier fluorinated analogs – CF_3. In general, since the frequencies of these six vibrations are close to match the gaps between the ground, first excited, and second excited doublets, the magnet performance could be improved by any structural modification that brought these vibrational modes out of resonance. All in all, everything suggests that there still exists further structural modification to explore in bis-metallocenium-based ligands, which seem to open more avenues in the pursuit of new highly-performing molecular magnets based on f-block elements.

ASSOCIATED CONTENT

AUTHOR INFORMATION

Corresponding Author

*E-mail for E.C.: eugenio.coronado@uv.es
*E-mail for J.J.B.: jose.baldovi@mpsd.mpg.de

ACKNOWLEDGMENT

The present work has been funded by the EU (COST Action CA15128 MOLSPIN and ERC-2014-CoG-647301 DECRESIM), the Spanish MINECO (Unit of Excellence “María de Maeztu” MdM-2015-0538, and grants MAT2017-89993-R and CTQ2017-89528-P) and the Generalitat Valenciana (Prometeo Program of Excellence). L. E.-M. also thanks the Generalitat Valenciana for a VALi+D predoctoral contract, J. J. B. acknowledges the EU for a Marie Curie Fellowship (H2020-MSCA-IF-2016-751047).

ABBREVIATIONS

(Word Style “Section_Content**”).** CCR2, CC chemokine receptor 2; CCL2, CC chemokine ligand 2; CCR5, CC chemokine receptor 5; TLC, thin layer chromatography.

REFERENCES

(Word Style "TF_References_Section"). References are placed at the end of the manuscript. Authors are responsible for the accuracy and completeness of all references. Examples of the recommended formats for the various reference types can be found at http://pubs.acs.org/page/4authors/index.html. Detailed information on reference style can be found in The ACS Style Guide, available from Oxford Press.

1

R. Sessoli, D. Gatteschi, A. Caneschi & M. A. Novak, *Nature*, 1993, **365**, 141-143.

2 L. Thomas, F. Lionti, R. Ballou, D. Gatteschi, R. Sessoli & B. Barbara, *Nature*, 1996, **383**, 145-147

3 Bagai, R.; Christou, G.; *Chem. Soc. Rev*., 2009, 38, 1011–1026

4 Bertaina, S.; Gambarelli, S.; Mitra, T.; Tsukerblat, B.; Müller, A.; Barbara, B.; Nature, 2008, 453, 203–206.

5 Leuenberger, M. N.; Loss, D.; *Nature*, 2001, *410*(6830), 789.

6 Troiani, F.; Affronte, M.; Chem. Soc. Rev., 2011, *40*(6), 3119-3129.

7 Bogani, L.; Wernsdorfer, W.; *Nanoscience And Technology: A Collection of Reviews from Nature Journals,* 2010, 194-201.

8 Gaita-Ariño, A.; Luis, F.; Hill, S.; Coronado, E; Nature Chem., 2019, 11(4), 301-309.

9

Waldmann, O.; *Inorg. Chem.* 2007, **46**, 10035-10037.

10 R.Bagai, G. Christou, *Chem. Soc. Rev.*, 2009, **38**, 1011-1026.

11 N. E. Chakov, S.- C. Lee, A. G. Harter, P. L. Kuhns, A. P. Reyes, S. O. Hill, N. S. Dalal, W. Wernsdorfer, K. A. Abboud, G. Christou, *J. Am. Chem. Soc.* 2006, **128**, 6975-6989.

12 C. J. Milios, A. Vinslava, W. Wernsdorfer, S. Moggach, S. Parsons, S. P. Perlepes, G. Christou, E. K. Brechin, *J. Am. Chem. Soc.*, 2007, **129**, 2754-2755.

13 K. Chakarawet, P. C. Bunting, J. R. Long, *J. Am. Chem. Soc.*, 2018, **140**, 2058-2061.

14

N. Ishikawa, M. Sugita, T. Ishikawa, S. Koshihara, Y. Kaizu, *J. Am. Chem. Soc.*, 2003, **125**, 8694-8695.

15 Meng, Y.-S.; Jiang, S.-D.; Wang, B.-W.; Gao, S.; *Acc. Chem. Res.,* 2016, 49,11, 2381-2389.

16 Woodruff, D.N.; Winpenny, R.E.P.; Layfield, R.A.; *Chem. Rev.* 2013, 113(7), 5110-5148

17

Craig, G.A.; Murrie, M.; Chem. Soc. Rev., 2015,44, 2135-2147

18 M. Feng, M. L. Tong, *Chem. Eur. J.*, 2018, **24**, 7574-7594.

19 J. M. Zadrozny, D. J. Xiao, M. Atanasov, G. J. Long, F. Grandjean, F. Neese, J. R. Long, *Nature Chemistry*, 2013, **5**, 577-581.

20 X.-N. Yao, J.-Z. Du, Y.-Q. Zhang, X.-B. Leng, M.-W. Yang, S.-D. Jiang, Z.-X. Wang, Z.-W. Ouyang, L. Deng, B.-W. Wang, et al. *J. Am. Chem. Soc.*, 2017, **139**, 373-380.

21 Rinehart, J. D.; Long, J. R.; J. Am. Chem. Soc. 2009, 131, 12558–12559

22 Moro, F.; Mills, D. P.; Liddle, S. T.; van Slageren, J.; *Angew. Chem. Int. Ed.* 2013, *52*(12), 3430-3433.

23 Baldoví, J. J.; Cardona-Serra, S.; Clemente-Juan, J. M.; Coronado, E.; Gaita-Ariño, A. *Chem. Sci.* 2013, 4, 938-946

24 Magnani, N.; Apostolidis, C.; Morgenstern, A.; Colineau, E.; Griveau, J.-C.; Bolvin, H.; Walter, O.; Caciuffo, R.; *Angew. Chem., Int. Ed.*, 2011, 50, 1696.

25 J. T. Coutinho, M. A. Antunes, L. C. J. Pereira, H. Bolvin, J. Marcalo, M. Mazzanti, M. Almeida, *Dalton Trans.*, 2012, **41**, 13568-13571.

26

27

K. L. M. Harriman, M. Murugesu, *Acc. Chem. Res.*, 2016, **49**, 1158-1167

28

H. Bolvin, *ChemPhysChem* 2009, **7**, 1575-1589

29

S. Gomez-Coca, E. Cremades, N. Aliaga-Alcalde, E. Ruiz, *J. Am. Chem. Soc.* 2013, **135**, 7010-7018

30

A. V. Palii, J. M. Clemente-Juan, E. Coronado, S. I. Klokishner, S. M. Ostrovsky, O.S. Reu, *Inorg. Chem.* 2010, **49**, 8073-8077

31

M. R. Pederson, S. N. Khanna, *Phys. Rev. B* 1999, **60**, 9566

32

H. A. Bethe, *Ann. Phys.*, 1929, **3**, 133–206.

33

J. D. Rinehart and J. R. Long, *Chem. Sci.*, 2011, **2**, 2078.

34

J. J. Baldoví, S. Cardona-Serra, J. M. Clemente-Juan, E. Coronado, A. Gaita-Ariño and A. Palii, *Inorg. Chem.*, 2012, **51**, 12565–12574.

35

J. J. Baldoví, S. Cardona-Serra, J. M. Clemente-Juan, E. Coronado, A. Gaita-Ariño and A. Palii, *J. Comput. Chem.*, 2013, **34**, 1961–1967.

36

N. F. Chilton, D. Collison, E. J. L. McInnes, R. E. P. Winpenny and A. Soncini, *Nat. Commun.*,

37

C. K. Jorgensen, R. Pappalardo and H.-H. Schmidtke, *J. Chem. Phys.*, 1963, **39**, 1422–1430.

38

W. Urland, *Chem. Phys.*, 1976, **14**, 393–401.

39

Malta, O. L.; *Chem. Phys. Lett.*, 1982, **87**, 27–29

40

Malta, O. L.; *Chem. Phys. Lett.*, 1982, **88**, 353–356.

41

P. Porcher, M. Couto Dos Santos and O. Malta, *Phys. Chem. Chem. Phys.*, 1999, **1**, 397–405.

42

J. J. Baldoví, J. J. Borrás-Almenar, J. M. Clemente-Juan, E. Coronado and A. Gaita-Ariño, *Dalton Trans.*, 2012, **41**, 13705.

43

J. J. Baldoví, L. E. Rosaleny, V. Ramachandran, J. Christian, N. S. Dalal, J. M. Clemente-Juan, P. Yang, U. Kortz, A. Gaita-Ariño and E. Coronado, *Inorg. Chem. Front.*, 2015, **2**, 893–897.

44

J. J. Baldoví, A. Gaita-Ariño, E. Coronado, *Dalton Trans.*, 2015, **44**, 12535-12538.

45

B. O. Roos, P. R. Taylor and P. E. M. Sigbahn, *Chem. Phys.*, 1980, **48**, 157–173.

46

P. Siegbahn, A. Heiberg, B. Roos and B. Levy, *Phys. Scr.*, 1980, **21**, 323–327.

47

P. E. M. Siegbahn, J. Almlöf, A. Heiberg and B. O. Roos, *J. Chem. Phys.*, 1981, **74**, 2384–2396.

48

F. Aquilante, L. De Vico, N. Ferré, G. Ghigo, P. Å. Malmqvist, P. Neogrády, T. B. Pedersen, M. Pitoňák, M. Reiher, B. O. Roos, L. Serrano-Andrés, M. Urban, V. Veryazov and R. Lindh, *J. Comput. Chem.*, 2010, **31**, 224–247.

49

G. Karlström, R. Lindh, P. Å. Malmqvist, B. O. Roos, U. Ryde, V. Veryazov, P. O. Widmark, M. Cossi, B. Schimmelpfennig, P. Neograd y and L. Seijo, in *Computational Materials Science*, 2003, vol. 28, pp. 222–239.

50

M. J. . T. Frisch G.W.; Schlegel, H. B.; Scuseria, G. E.; Robb, M. A.; Cheeseman, J. R.; Scalmani, G.; Barone, V.;Mennucci, B.; Petersson, G. A.; Nakatsuji, H.; Caricato, M.; Li, X.; Hratchian, H. P.; Izmaylov, A. F.; Bloino, J.; Zheng, G.; Sonnenber, D. J, *Gaussian, Inc. Wallingford CT*, 2009, 2–3.

51

F. Neese, *Wiley Interdiscip. Rev. Comput. Mol. Sci.*, 2012, **2**, 73–78.

52

H. J. Werner, P. J. Knowles, G. Knizia, F. R. Manby and M. Schütz, *Wiley Interdiscip. Rev. Comput. Mol. Sci.*, 2012, **2**, 242–253.

53

P. P. Hallmen, C. Köppl, G. Rauhut, H. Stoll and J. van Slageren, *J. Chem. Phys.*, 2017, **147**, 164101.

54

S. Calvello, M. Piccardo, S. V. Rao and A. Soncini.

55

L. Ungur and L. F. Chibotaru, *Phys. Chem. Chem. Phys.*, 2011, **13**, 20086.

56

R. J. Blagg, L. Ungur, F. Tuna, J. Speak, P. Comar, D. Collison, W. Wernsdorfer, E. J. L. McInnes, L. F. Chibotaru and R. E. P. Winpenny, *Nat. Chem.*, 2013, **5**, 673–678.

57

Y. N. Guo, G. F. Xu, W. Wernsdorfer, L. Ungur, Y. Guo, J. Tang, H. J. Zhang, L. F. Chibotaru and A. K. Powell, *J. Am. Chem. Soc.*, 2011, **133**, 11948–11951.

58

L. F. Chibotaru and L. Ungur, *J. Chem. Phys.*, , DOI:10.1063/1.4739763.

59

G. Cucinotta, M. Perfetti, J. Luzon, M. Etienne, P. E. Car, A. Caneschi, G. Calvez, K. Bernot and R. Sessoli, *Angew. Chem. - Int. Ed.*, 2012, **51**, 1606–1610.

60

M. E. Boulon, G. Cucinotta, J. Luzon, C. Degl'Innocenti, M. Perfetti, K. Bernot, G. Calvez, A. Caneschi and R. Sessoli, *Angew. Chem. - Int. Ed.*, 2013, **52**, 350–354.

61

M. Speldrich, J. van Leusen, P. Kögerler, *J. Comput. Chem.*, 2018, **39**, 2133-2145.

62

McAdams, S. G.; Ariciu, A. M.; Kostopoulos, A. K.; Walsh, J. P.; Tuna, F.; *Coord. Chem. Rev.*, 2017, *346*, 216-239.

63

Meihaus, K.R.; Long, J.R.; Dalton Trans., 2016, 44(6), 2517-2528.

64

C.A.P. Goodwin, F. Ortu, D. Reta, N.F. Chilton, *Nature*, 2017, **548**, 439-442.

65

L. Escalera-Moreno, J. J. Baldoví, A. Gaita-Ariño, E. Coronado, *Chem. Sci.*, 2018, **9**, 3265-3275.

66

(a) L. Escalera-Moreno, N. Suaud, A. Gaita-Ariño, E. Coronado, 2015, arXiv:1512.05690v1 (b) L. Escalera-Moreno, N.Suaud, A. Gaita-Ariño, E. Coronado, *J. Phys. Chem. Lett.*, 2017, **8**, 1695-1700.

67

A. Lunghi, F. Totti, R. Sessoli, S. Sanvito, *Nat. Commun.* 2017, **8**, 14620.

68

A. Lunghi, F. Totti, S. Sanvito, R. Sessoli, *Chem. Sci.*, 2017, **8**, 6051-6059.

69

M. Atzori, L. Tesi, S. Benci, A. Lunghi, R. Righini, A. Taschin, R. Torre, L. Sorace, R. Sessoli, *J. Am. Chem. Soc.*, 2017, **139**, 4338-4341.

70

A. Albino, S. Benci, L. Tesi, M. Atzori, R. Torre, S. Sanvito, R. Sessoli, A. Lunghi, 2019, arXiv:1904.04922.

71

A. Lunghi, S. Sanvito, 2019, arXiv:1903:01424.

72

L. Escalera-Moreno, J. J. Baldoví, E. Coronado, 2019, arXiv:1905.06989

73

Yang, J.-W.; Tian, Y.-M.; Tao, J.; Chen, P.; Li, H.-F.; Zhang, Y.-Q.; Yan, P.F.; Sun, W.-B., Inorg. Chem. 018, 57, 8065-8077.

74 Coutinho, J. T.; Perfetti, M.; Baldoví, J. J.; Antunes, M. A.; Hallmen, P. P.; Bamberger, H.; Crassee, I.; Orlita, M.; Almeida, M.; van Slageren, J.; Pereira, L. C. J. Chem. Eur. J. 2019, 25(7), 1758-1766.

75

Antunes, M. A.; Coutinho, J. T.; Santos, I. C.; Marçalo, J.; Almeida, M.; Baldoví, J. J.; Pereira, L. C. J.; Gaita-Ariño, A.; Coronado, E. Chem. Eur. J. 2015, 21(49), 17817-17826.